

**Multiwavelength Characterization of a Dynamically Relaxed Cool Core Galaxy Cluster at  $z = 1.5$** 

ANTHONY M. FLORES ,<sup>1, 2, 3, 4</sup> ADAM B. MANTZ ,<sup>3</sup> STEVEN W. ALLEN ,<sup>2, 3, 4</sup> R. GLENN MORRIS ,<sup>3, 4</sup>  
ABIGAIL Y. PAN ,<sup>2, 3</sup> TAWEEWAT SOMBOONPANYAKUL ,<sup>3, 5</sup> HALEY R. STUEBER ,<sup>2, 3</sup> AND MICHAEL McDONALD ,<sup>6</sup>

<sup>1</sup>Department of Physics and Astronomy, Rutgers University, 136 Frelinghuysen Rd, Piscataway, NJ 08854, USA

<sup>2</sup>Department of Physics, Stanford University, 382 Via Pueblo Mall, Stanford, CA 94305, USA

<sup>3</sup>Kavli Institute for Particle Astrophysics and Cosmology, 452 Lomita Mall, Stanford, CA 94305, USA

<sup>4</sup>SLAC National Accelerator Laboratory, 2575 Sand Hill Road, Menlo Park, CA 94025, USA

<sup>5</sup>Department of Physics, Faculty of Science, Chulalongkorn University, 254 Phayathai Road, Patumwan, Bangkok 10330, Thailand

<sup>6</sup>MIT Kavli Institute for Astrophysics and Space Research, Massachusetts Institute of Technology, Cambridge, MA 02139, USA

(Received November 11, 2025; Revised January 30, 2026; Accepted February 13, 2026)

**ABSTRACT**

We present imaging and spectroscopic analyses of Chandra and XMM-Newton observations of ACT-CL J0123.5–0428, one of the most massive, highest redshift galaxy clusters detected within the survey fields of the Atacama Cosmology Telescope. The Chandra data are sufficient to characterize the morphology of this cluster and constrain the geometrically deprojected temperature in 2 spatial bins out to  $r_{2500}$ , revealing a dynamically relaxed system whose temperature drops to  $kT = 1.8 \pm 0.6$  keV in the inner  $\sim 40$  kpc. Within this same inner radius, the surface brightness and density of the ICM is sharply peaked, and the cooling time falls to  $t_{\text{cool}} = 280_{-120}^{+150}$  Myr. A novel forward-modeling analysis of the XMM data extends imaging and spectroscopic measurements of this system out to  $r_{500}$ , constraining the redshift to  $z = 1.50 \pm 0.03$ , with a mean temperature of  $kT = 7.3 \pm 1.1$  keV and an emission-weighted mean metallicity of  $Z/Z_{\odot} = 0.43_{-0.25}^{+0.46}$ . We also utilize the limited optical/IR photometric coverage of the cluster to characterize the properties of the brightest cluster galaxy (BCG), which is coincident with the X-ray peak. Despite the high redshift and strong cool core, the BCG exhibits no signs of recent or ongoing star formation, suggesting AGN feedback has been acting persistently to stem star formation since  $z \sim 2.5$ . These measurements identify ACT-CL J0123.5–0428 as the highest redshift, dynamically relaxed, cool core galaxy cluster discovered to date, making it a premier target for future astrophysical and cosmological studies.

**1. INTRODUCTION**

Galaxy clusters are the pinnacle of cosmic structure formation. These gigantic systems, which grow continuously via accretion from their surrounding environments and the sporadic merging of larger substructures, have proven to be exceptionally useful for both astrophysical and cosmological studies. The matter content of galaxy clusters is approximately 5/6 dark matter, with the remaining  $\sim 1/6$  being baryonic, primarily in the hot X-ray emitting intracluster medium (ICM; see Voit 2005; Böhringer & Werner 2010; Allen, Evrard, & Mantz 2011; Kravtsov & Borgani 2012; Walker et al. 2019; Allen & Mantz 2019 for reviews).

Among the broader population of galaxy clusters, the most dynamically relaxed systems – those that have not undergone recent subcluster merger events – are

of particular interest. For these systems, within a few sound crossing times, the ICM will approach hydrostatic equilibrium, adopting symmetric (approximately ellipsoidal) configurations. This geometric simplicity makes relaxed clusters particularly powerful as cosmological probes, allowing straightforward measurements of the three-dimensional gas and total matter properties (Allen, Evrard, & Mantz 2011). Measurements of the evolution of gas mass fraction and thermodynamic properties of such clusters have been used to place powerful constraints on cosmology (Allen et al. 2002, 2004, 2008; Mantz et al. 2014, 2022; Schmidt et al. 2004; Wan et al. 2021; see also Ettori et al. 2009; Bonamente et al. 2006; Kozmanyan et al. 2019 for studies not exclusively using relaxed systems) and the properties of dark matter (Amodeo et al. 2016; Mantz et al. 2016a; Darragh-Ford et al. 2023).

As clusters transition to this dynamically relaxed state, their atmospheres stratify, with the coolest, dens-

est, lowest entropy and typically highest metallicity gas sinking towards the cluster core. This leads to a characteristic sharp, central peak in the X-ray surface brightness, a drop in central temperature, and, commonly, metallicity gradients. The cooling times at the centers of these so-called “cool core” clusters are typically significantly less than a Hubble time (often of the order a few  $10^8$  yr or less, with the measurements generally limited by instrument spatial resolution; e.g. [White et al. 1997](#); [Peres et al. 1998](#); [Allen 2000](#)) and, in the absence of a balancing heat source, these regions should rapidly undergo runaway cooling (see [Fabian 1994](#) for a review). However, while the central galaxies of some cool core clusters indeed host large reservoirs of cold gas and vigorous, ongoing star formation ([Crawford et al. 1999](#); [Edge 2001](#); [Cavagnolo et al. 2008](#); [Voit et al. 2008](#); [O’Dea et al. 2008](#); [Donahue et al. 2010](#); [Edge et al. 2010](#); [McDonald et al. 2015](#); [Olivares et al. 2019](#)) generally, the amounts of cold gas and star formation observed lie far below the runaway cooling expectations, with some of the most dynamically relaxed cool core systems (of which [Abell 2029](#) is a notable low redshift example) showing no measurable cold gas buildup or associated recent star formation ([Martz et al. 2020](#)). In these systems, active galactic nucleus (AGN) feedback, which inflates cavities and drives shocks, sound waves and turbulence into the surrounding intracluster medium (ICM) appears able to effectively stem cooling and prevent star formation. Remarkably, these feedback processes also appear to limit the accretion rates onto the central black holes to allow just enough heat to be deposited into the surrounding ICM to keep the central regions of cool core clusters in an approximately steady state, for periods of up to billions of years ([McNamara & Nulsen 2007, 2012](#); [Fabian 2012](#); [Zhuravleva et al. 2014](#); [Li et al. 2015](#); [Yang & Reynolds 2016](#); [Li et al. 2017](#); [Ehler et al. 2023](#)). A key question at this point is when this particular form of AGN feedback, often referred to as mechanical or radio mode feedback, first began to be important in shaping the properties of cluster cool cores.

A key limitation affecting such studies is the dearth of confirmed dynamically relaxed, cool core clusters at high redshift. Specifically, using the quantitative X-ray morphological metrics of [Mantz et al. 2015](#), only 3 such systems at  $z \gtrsim 1$  have been previously confirmed using deep X-ray observations ([Mantz et al. 2022](#)), with the most distant system, SPT-CL J2215–3537, at  $z = 1.16$  ([Mantz et al. 2022](#); [Calzadilla et al. 2023](#); [Stueber et al. 2026](#)). Efforts to expand these studies to higher redshifts have been challenged both by the relatively small samples of high redshift clusters known in general, and by the faint X-ray fluxes of these targets, which make

detailed X-ray characterization expensive. Fortunately, the advent of cluster catalogs based on measurements of the thermal Sunyaev-Zel’dovich (SZ; [Sunyaev & Zeldovich 1972](#)) effect is addressing the former issue. Compared to X-ray and optical measurements, the SZ effect is insensitive to the redshift of a cluster, making the detection of the most massive systems at high redshift relatively straightforward. In particular, the South Pole Telescope (SPT) and Atacama Cosmology Telescope (ACT) have observed over 5,000 and 13,000 square degrees of the southern sky, respectively, finding thousands of clusters in total, including more than 200 at  $z > 1$  ([Figure 1](#); [Bleem et al. 2015, 2020](#); [Huang et al. 2020](#); [Hilton et al. 2021](#)). Although the SZ maps from SPT and ACT do not generally provide meaningful morphological information, targeted X-ray follow-up of these systems has proven an effective way to identify and characterize high mass, high redshift dynamically relaxed systems and the properties of their central ICM and galaxies (e.g. [McDonald et al. 2013](#); [Hlavacek-Larrondo et al. 2015](#); [McDonald et al. 2019](#); [Ruppin et al. 2021, 2023](#); [Calzadilla et al. 2023, 2024](#)).

Here, we present the multiwavelength characterization of ACT-CL J0123.5–0428 (hereafter ACT-CL J0123), identifying it has the highest redshift, dynamically relaxed, cool core galaxy cluster discovered to date. With a total mass estimate of  $M_{500} = 3.6_{-0.6}^{+0.7} \times 10^{14} M_{\odot}$ <sup>7</sup> based on its SZ survey detection ([Hilton et al. 2021](#)), ACT-CL J0123 is one of the most massive, highest redshift galaxy clusters known ([Figure 1](#)). Initially, the cluster was inferred to have a photometric redshift of  $z_{\text{phot}} = 1.43 \pm 0.03$  from ground-based optical/near-IR survey coverage (DECALS; [Dey et al. 2019](#)). Here, we use X-ray measurements to determine a spectroscopic redshift of  $z = 1.50 \pm 0.03$ . Our study utilizes newly developed methods for the analysis of Chandra and XMM-Newton observations to jointly characterize both the small- and large-scale physics of the X-ray emitting intracluster medium (ICM). We also utilize the aforementioned archival optical and near-IR photometry to probe the history of star formation within the central brightest cluster galaxy.

Unless otherwise noted, all measurements are reported as the mode and associated 68.3% credible intervals corresponding to the highest posterior probability density. We assume a flat  $\Lambda$ CDM cosmology with  $H_0 = 70$

<sup>7</sup>  $M_{500}$  is defined as the mass enclosed within a sphere of radius  $r_{500}$ , the radius at which the mean density of the cluster exceeds the critical density of the Universe  $\rho_{\text{crit}}(z)$  by a factor of 500. For any given overdensity,  $\Delta$ ,  $M_{\Delta}$  is given by:  

$$M_{\Delta} = \frac{4}{3}\pi\Delta\rho_{\text{crit}}(z)r_{\Delta}^3.$$

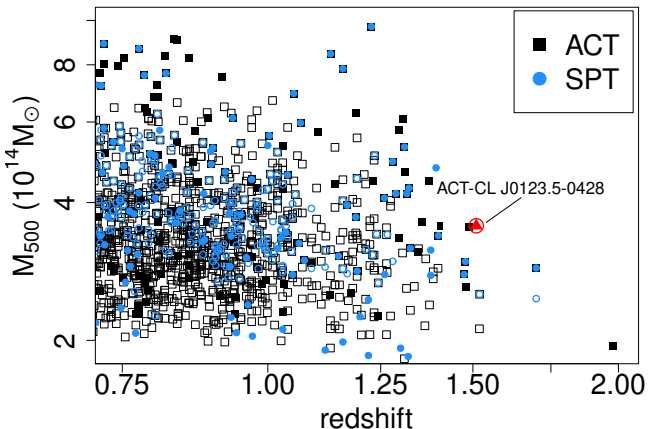


**Figure 1.** SZ cluster detections from the Atacama Cosmology Telescope (ACT; Hilton et al. 2021) and the South Pole Telescope (SPT; Bleem et al. 2015, 2020; Huang et al. 2020), limited to  $z > 0.7$  and  $S/N > 5$ . Filled markers represent systems with targeted X-ray observations as of Chandra Cycle 27/XMM Cycle 24.

$\text{km s}^{-1} \text{Mpc}^{-1}$ ,  $\Omega_m = 0.3$ , and  $\Omega_\Lambda = 0.7$ . At our reference redshift of  $z = 1.50$ , the angular sizes of  $1''$  and  $1'$  respectively correspond to 8.46 kpc and 508 kpc in physical scale. Metallicities are reported relative to Solar abundance measurements of Asplund et al. (2009).

## 2. DATA

ACT-CL J0123 was observed at X-ray wavelengths as part of a joint Chandra+XMM-Newton campaign targeting the highest mass, highest redshift clusters in the Advanced ACTPol cluster catalog. We obtained one Chandra observation of ACT-CL J0123 (OBSID 26940; clean exposure 51.2ks) using the ACIS-S camera. This observation is available on the Chandra Data Archive (CDA)<sup>8</sup> via doi:10.25574/cdc.529. These data were reprocessed using version 4.16 of the Chandra software analysis package, CIAO<sup>9</sup>, and version 4.11.0 of the Chandra Calibration Database, CALDB<sup>10</sup>. Automated lightcurve cleaning of the event file to remove periods of enhanced background was performed following the techniques recommended in the ACIS data processing guide<sup>11</sup>.

In contrast to the relatively clean Chandra observation, our XMM observations were heavily ( $\sim 60\%$ ) flared, resulting in a clean exposure time of 15/12ks in MOS/pn, respectively. These data are available on the ESA XMM-Newton Science Archive (OBSID

0914590601)<sup>12</sup>. The XMM data were reduced using the standard Source Analysis Software (SAS; version 18.0.0)<sup>13</sup> tools following the guidance in the Extended Source Analysis Software (XMM-ESAS) cookbook<sup>14</sup>. After an initial round of automated filtering, we inspected each detector’s lightcurve manually to identify and remove additional periods of flaring missed by the automated MOS-FILTER and PN-FILTER steps.

The X-ray images of ACT-CL J0123 from Chandra and XMM are shown in Figure 2. After lightcurve filtering, a simple  $\beta$ -model + background fit to the images from each instruments reveal the Chandra observation obtained roughly 500 net cluster counts (0.6–7.0 keV), while the XMM observation obtained  $\sim 700$  (0.4–4.0 keV). Over these respective energy bands, this corresponds to a measured cluster signal of  $\sim 50\%$  of the total background level in Chandra compared to a measured cluster signal of  $\gtrsim 2\times$  the total background level in XMM. From the Chandra image (as it is both higher resolution and exhibits less PSF blending in the cluster core compared to XMM), we obtained the cluster center from the Symmetry, Peakiness, and Alignment (SPA; Mantz et al. 2015) algorithm, which iteratively finds the median photon position after background subtraction. We adopt this center ( $\alpha = 1^{\text{h}}23^{\text{m}}32\text{s}098$ ,  $\delta = -4^{\circ}28'25\text{.}320$ ; J2000) as the cluster center in all subsequent analyses.

Beyond these X-ray observations, ACT-CL J0123 does not yet have targeted multiwavelength follow-up, though it does have coverage from multiple ground- and space-based surveys. The photometric redshift was determined from the Dark Energy Camera Legacy Survey (DECaLS; Dey et al. 2019) from which it is also possible to visually identify the Brightest Cluster Galaxy (BCG), which is coincident with the center of the X-ray gas<sup>15</sup> (see Fig 2). At this same position, coverage from the Very Large Array Sky Survey (VLASS) does not indicate any bright radio source near the location of the BCG, with epoch 3.1 observations placing a  $1\sigma$  limit on this nondetection at  $69\mu\text{J}$  in the 2–4 GHz band (5–10 GHz rest frame). Similarly, data from the Wide-field Infrared Survey Explorer (WISE) do not identify the BCG itself as an AGN, as the WISE color ( $W_1 - W_2$ )<sub>AB</sub> = 0.06 is too low to indicate an AGN at these redshifts (Sombroek et al. 2022). ACT-CL J0123 lacks any optical/IR spectra to precisely determine a spectroscopic redshift. To that end, the X-ray data can be used to

<sup>8</sup> <https://cxc.harvard.edu/cda/>

<sup>9</sup> <http://cxc.harvard.edu/ciao/>

<sup>10</sup> <https://cxc.harvard.edu/caldb/>

<sup>11</sup> [https://cxc.harvard.edu/ciao/guides/acis\\_data.html](https://cxc.harvard.edu/ciao/guides/acis_data.html)

<sup>12</sup> <https://nxsa.esac.esa.int/nxsa-web/>

<sup>13</sup> <https://www.cosmos.esa.int/web/xmm-newton/sas>

<sup>14</sup> <https://heasarc.gsfc.nasa.gov/docs/xmm/esas/cookbook/>

<sup>15</sup> The optical BCG position is less than  $1''$  from the SPA center, and within the SPA  $1\sigma$  uncertainties shown in Figure 2.

constrain the redshift based primarily on the iron  $K\alpha$  line complex around 6.7 keV (rest frame), albeit at CCD spectral resolution.

### 3. X-RAY METHODS AND MODELING

Our spectral modeling of ACT-CL J0123 generally followed the forward modeled approach to Chandra and XMM observations described in Mantz et al. (2025); hereafter M25. This approach was designed to provide the best statistical description of faint cluster environments by identifying point sources, and explicitly forward-modeling the soft foreground, unresolved X-ray background/residual AGN contamination and detector-specific non-X-ray backgrounds. Below, we briefly summarize these methods and describe their specific application to the short Chandra+XMM exposures available for ACT-CL J0123. For our spectral analyses, all spectra were modeled using the XSPEC<sup>16</sup> analysis package (version 12.12.1c), and all thermal models are described by APEC plasma models (Smith et al. 2001; ATOMDB version 3.0.9) (i.e. a single temperature, metallicity and density). Photoelectric absorption from gas in our own galaxy was fixed to a hydrogen column density of  $3.57 \times 10^{20} \text{ cm}^{-2}$  (HI4PI Collaboration et al. 2016), and we used the cross sections of Balucinska-Church & McCammon (1992). Unless otherwise stated, we constrained model parameters using the LMC<sup>17</sup> Markov Chain Monte Carlo (MCMC) code, with the likelihood given by the C-statistic in XSPEC (Cash 1979; Arnaud 1996). Because this approach is fully forward modeled, we were able to use the original Cash Statistic to account for the Poisson nature of the counts without grouping spectral channels.

#### 3.1. Point Sources

Contaminating point sources were identified via the CIAO tool WAVDETECT<sup>18</sup> run on broadband (0.6–7.0 keV) native resolution (0.492''/pixel) Chandra images. These point sources were masked in Chandra analyses using a circular mask of radius 4 times larger than the size of the the Chandra PSF corresponding to an enclosed count fraction (ECF) of 0.393<sup>19</sup>. We resized these masks for XMM data based on the flux characterization returned by WAVDETECT and a model for the XMM PSF (Read et al. 2011) to limit the residual contaminating surface brightness from each source

to  $\lesssim 5 \times 10^{-19} \text{ ergs/s/cm}^2/\text{arcsec}^2$  (unabsorbed 2–10 keV band) following the approach used in Mantz et al. (2020) and Flores et al. (2021). For the bright AGN  $\sim 20''$  northwest of the cluster center (Fig 2), this default XMM mask size would have removed nearly half of all counts from the cluster. Instead, for this source, the brightest X-ray emission was masked using a 17'' radius circle centered on the Chandra detection, with the heightened residuals from the wings of the PSF (compared to the standard procedure) accounted for in our imaging and spectral modeling (see below). For point sources in the XMM data beyond the ACIS-S footprint, we conducted a second run of WAVDETECT on the 0.4–4.0 keV pn image assuming a constant XMM PSF of 6'' full width at half maximum (FWHM) across the FOV. We produced circular masks with the radius given by the semi-major axis of the elliptical regions returned by WAVDETECT. We found that this method produces masks that are typically just as conservative as the masks produced for regions with joint Chandra coverage.

#### 3.2. X-ray Spectral Methods

As described in M25, we build and validate an initial model for various X-ray foregrounds and backgrounds (namely the soft X-ray foreground and unresolved cosmic X-ray background) by considering regions on the Chandra ACIS and XMM-Newton EPIC detectors free from cluster emission (hereafter, the “offcluster” regions). These regions are also fitted simultaneously with cluster spectra in later stages of the analysis, largely to help constrain the strength of the various components (see below). In both instruments, we excluded a circle of radius 3' ( $> 2 r_{500}$ ) to mask the entirety of the ICM. In Chandra, a significant portion of S3, in addition to all of CCDs S2 and S1, were free of any cluster emission and were used for the offcluster analysis. For XMM, we defined a large circular region extending 12' in radius, excluding the same 3' radius circle centered on the cluster. The outer radius was selected to encompass as much of the field of view as possible while reducing errors from systematic uncertainties due to vignetting (i.e. error in the calibration of the effective area at large off axis angles; Urban et al. 2011).

Our spectral model for the soft X-ray foreground (primarily emission from the Milky Way halo and Local Hot Bubble) comes from fits of a combination of absorbed and unabsorbed thermal models to the ROSAT All Sky Survey (RASS) maps (Snowden et al. 1995, 1997) in an offcluster region. In Chandra, we applied this model as-is, marginalizing over a 3.5% Gaussian prior on its normalization to describe the statistical un-

<sup>16</sup> <https://heasarc.gsfc.nasa.gov/docs/xanadu/xspec/>

<sup>17</sup> <https://github.com/abmantz/lmc>

<sup>18</sup> <https://cxc.cfa.harvard.edu/ciao/ahelp/wavdetect.html>

<sup>19</sup> An ECF of 0.393 provides the integrated  $1\sigma$  volume of a 2-D Gaussian

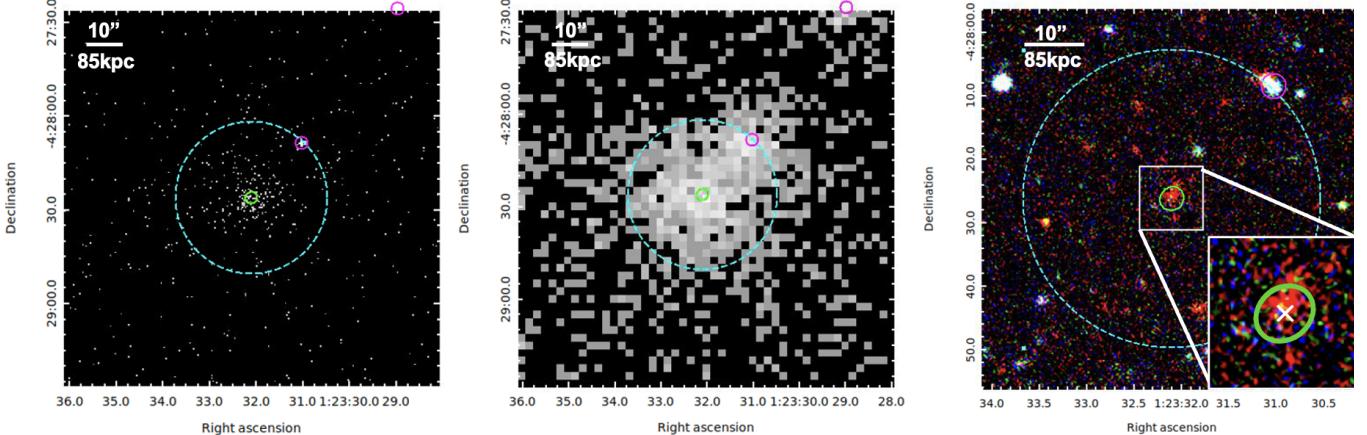


**Figure 2.** X-ray and optical images of ACT-CL J0123.5–0428. *Left:* Soft band (0.6–2.0 keV) 51.2ks Chandra image. *Center:* 0.4–4.0 keV stacked XMM Newton image of 15ks (MOS1/2) and 11.6ks (pn). *Right:* Legacy Survey DR10  $g, r, z$  image cutout of ACT-CL J0123. In each image, the  $1\sigma$  uncertainty in the position of the cluster center (from the Chandra data) is marked with a green ellipse. Point sources identified with the CIAO tool WAVDETECT are marked with magenta circles of radius 2''. The measured value of  $r_{2500}$  is denoted by the dashed cyan circle (See Section 4.3). A 10'' cutout of the center of the optical image is presented to highlight the alignment of the BCG with the X-ray cluster center (white cross).

certainty in the ROSAT fit. In XMM, we recognized that we have superior sensitivity and spectral resolution, so the foreground model applied to XMM spectra dropped an absorbed 0.1keV thermal model in favor of the AtomDB Charge Exchange model (ACX; Smith et al. 2014) designed to account for charge exchange in the solar wind that can contribute significantly to soft emission. Following M25, we also specifically tested for the preference of a warmer ( $\sim 0.75$ keV) absorbed thermal component, which we found ACT-CL J0123 statistically prefers. Once the best-fitting foreground parameters (i.e. temperatures and normalizations of the APEC/ACX components) were determined for the XMM offcluster region, they were fixed for later stages of the analysis. When applying this model simultaneously to smaller regions that include cluster emission, the normalizations were scaled by the ratio in area to the offcluster region, and an overall constant scaling was applied to all regions as a free parameter..

In addition to the residual emission from masked, detected sources due to the wings of the XMM PSF, we also predicted the contribution from the unresolved (i.e. not detected by Chandra) cosmic X-ray background following the same methods outlined in M25. In brief, MARX simulations of sources located at increasing off-axis angles provide sensitivity limits (at the 99% level) for the detection of point sources as a function of source flux, distance from the Chandra aimpoint (i.e. Chandra PSF size), and “background” level (including ICM emission for point sources within the cluster or in projection). Assuming an AGN X-ray luminosity function (Miyaji et al. 2015), we obtained the total expected contribu-

tion from unresolved AGN in each pixel by integrating this luminosity function up to the flux corresponding to our sensitivity limits. In our spectral analyses, the unresolved and residual AGN components were modeled by a single absorbed powerlaw with a photon index of 1.4. The normalization of this powerlaw in each spatial region was fixed to the total expectation from the methods described above, with an overall scaling shared between spatial regions. For XMM, a significant portion of the offcluster region was outside the Chandra FOV. Masks applied to sources identified in these data were independent of Chandra, thus our Chandra PSF-dependent sensitivity model was invalid. In this case, the normalization of the powerlaw model was not fixed to any expectation, nor was it linked to the models of other simultaneously-modeled regions.

We generated models to describe the quiescent particle background (QPB) in both telescopes, following the work of Suzuki et al. (2021) for Chandra ACIS and using the ESAS MOS-BACK and PN-BACK tools for XMM EPIC. Both methods provide an observation-specific spatially varying model of the X-ray particle background to be forward modeled into our spectral analyses. In Chandra, these models are specific to each detector, using the high-energy count rate to scale the expected spectrum. Each Chandra QPB model was marginalized over the statistical uncertainty in the normalization, with an additional 5% allowance overall to account for additional systematics. In XMM, the ESAS QPB model spectrum is converted to an XSPEC table model with fixed shape but free normalization. Instead of allowing this normalization to vary for each spatial region

fit, we fixed the relative normalizations of each region given by the ESAS model expectation and introduced a single constant scaling factor specific to each detector (MOS1, MOS2, and pn). Each of these detector-specific scalings was marginalized over an independent 10% Gaussian prior.

Finally, we used the same methods as M25 to produce a smooth model for the pn Out-of-Time (OOT) events. The same SAS tools that produce science spectra also provide an estimate of the shape of the OOT spectrum by resampling the events in the readout direction. We fit this spectrum with a combination of 2 absorbed powerlaws, 2 Gaussians, and the smoothed QPB model described above. One pair of powerlaw+Gaussian components is folded through the instrumental response (ARF) while the other is not. This process is not designed to describe any physical process, but instead provide an estimate of the spectral shape of OOT events (see M25 for further details and examples). The normalizations of each component in the OOT model were fixed and scaled by a constant value of 0.063 (appropriate for Full Frame mode observations) in all spectral analyses.

In Chandra, the default energy range of our fits was 0.6–7.0 keV. For regions containing cluster emission that were dominated by the particle background (i.e. at large radius), we narrowed the energy bounds of our fits to match the energies at which the cluster signal is higher than the particles. In XMM, we fit from 0.4–12.0 keV in MOS1/2 and 0.4–15.0 keV in pn, excluding 1.2–1.9 keV for both MOS detectors to remove the Al and Si fluorescence lines, and 1.2–1.65 keV in pn to remove the Al line. Similarly, we exclude 7.0–10.0 keV to exclude the Ni, Cu, and Zn fluorescence lines. While the 10.0–15.0 keV band is devoid of any cluster signal, it was especially useful to normalize the particle background and to test for the presence of residual soft protons, for which we saw no visual evidence.

## 4. RESULTS

### 4.1. Cluster Morphology

At such high redshift, the HPD of the XMM PSF spreads emission over an area greater than 120kpc in scale, significantly complicating small-scale probes of the ICM surface brightness distribution, particularly the peakiness of the profile. Therefore, the physics of the core and overall morphology of ACT-CL J0123 were entirely constrained by the Chandra data. To determine the morphology of ACT-CL J0123, we computed the SPA metrics from the soft-band (0.6–2.0 keV) Chandra image and bootstrapped this computation 10,000 times to obtain an estimate of the error on each morphological parameter. The SPA metrics calculated for

ACT-CL J0123 ( $s = 1.3 \pm 0.2$ ,  $p = -0.7 \pm 0.2$ , and  $a = 1.3 \pm 0.2$ ) are plotted in Fig. 3 alongside those of other dynamically relaxed and unrelaxed systems. ACT-CL J0123 met the SPA criteria for relaxation ( $> 50\%$  of bootstrap measurements simultaneously satisfying  $s > 0.87$ ,  $p > -0.82$ , and  $a > 1.0$ ; Mantz et al. 2015).

### 4.2. Redshift

As ACT-CL J0123 currently lacks optical/near-IR spectroscopic follow-up of its cluster members, we used the XMM data to constrain its redshift. We extracted a single spectrum from an 80'' circle surrounding the cluster center, corresponding to the extent of detected cluster emission in the XMM observation and fit a single absorbed thermal model (PHABS×APEC). We found the best-fit spectroscopic redshift of  $z_{\text{spec}} = 1.50 \pm 0.03$ , and fixed the value at  $z = 1.50$  in all later stages of analysis. The spectrum used to determine the redshift, the best fit model (including individual model components to highlight their relative strengths), and the model residuals are presented in Figure 4.

### 4.3. Annular Deprojection

To produce radial profiles (e.g. gas density or temperature), we extracted spectra in concentric annuli surrounding the cluster center. The modeling of these data accounted for both the geometric effect of the projection of emission from spherical shells onto circular annuli of smaller radius and the mixing of emission between annuli due to the instrumental PSF. (Fabian et al. 1981; Kriss et al. 1983). In our Chandra analysis, this took the form of the PROJCT model which accounts for the geometric mixing ignoring the negligible effects of the Chandra PSF. In XMM where the mixing from the PSF is significantly more pronounced, we explicitly calculated a matrix of mixing values that accounts for effects of both geometric projection and the PSF to describe how the emission from a given annulus is spread into all others. To predict the spread of cluster emission by the PSF, we used the best-fit parameters of a  $\beta$ -model fit to the Chandra data where PSF mixing is minimal (Mantz et al. 2020). To obtain the gas density profile for the cluster, we converted the model normalizations<sup>20</sup> to ICM density using the canonical mean molecular mass of  $\mu = 0.61m_p$ , our reference cosmology, and the cluster redshift  $z = 1.5$ . The final bin of the Chandra and

<sup>20</sup> The normalization of the APEC model is defined as  $\frac{10^{-14}}{4\pi D_A(1+z)^2} \int n_e n_H dV$  and is therefore a proxy for the emissivity of the gas from which we can recover the gas electron density.

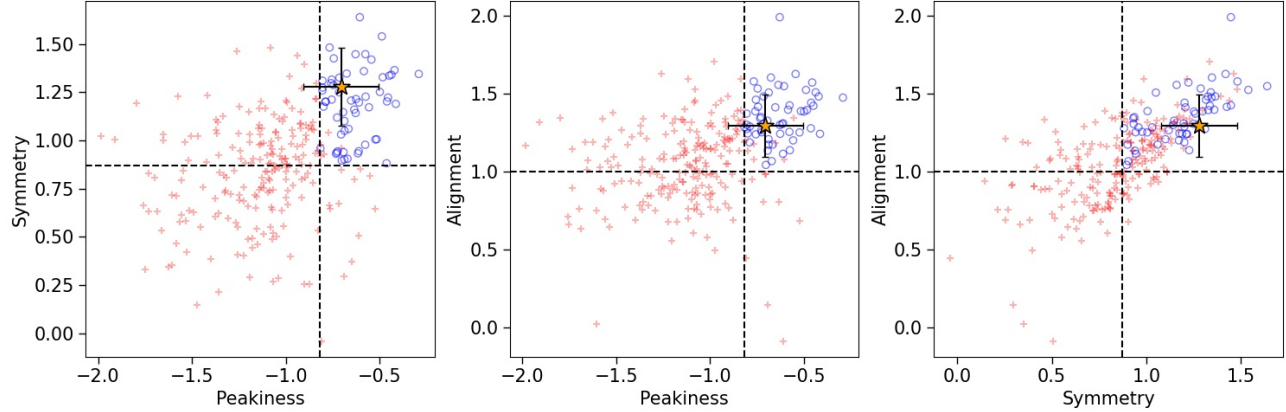


**Figure 3.** Symmetry, Peakiness and Alignment metrics describing the X-ray morphology of ACT-CL J0123, compared with a large sample of clusters (Mantz et al. 2015). ACT-CL J0123 (orange star) satisfies the criteria for relaxation, which is defined in terms of exceeding thresholds (dashed lines) in all 3 parameters. For the larger sample, blue circles (red crosses) show clusters classified as relaxed (unrelaxed).

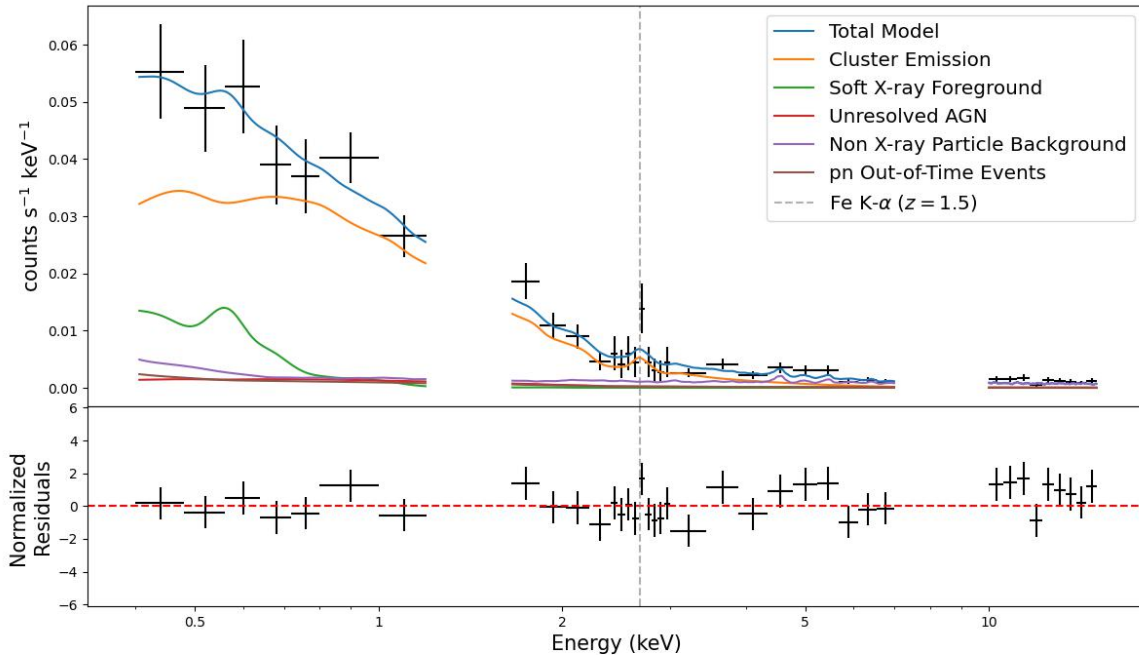


**Figure 4.** *Top:* pn spectrum of ACT-CL J0123, extracted from a circular region of radius  $80''$  centered on the cluster. The spectrum is binned in energy for clarity, with a finer binning around 2.7 keV (6.7 keV rest frame) to highlight the Fe K- $\alpha$  detection. The vertical dashed grey line indicates Fe K- $\alpha$  emission redshifted by  $z_{\text{spec}} = 1.5$ . Also plotted are the total model (blue) and individual model components, including the cluster (orange), X-ray foreground (green), cosmic X-ray background (red), quiescent particle background (QPB; purple) and pn out-of-time (OOT) events (brown). Gaps in the model curves and between data points correspond to the excluded energies in our fits due to fluorescence lines. *Bottom:* Best-fit model residuals to the pn data, normalized by their uncertainty.

XMM profiles is corrected for potential emission mixing in from beyond the outermost spectral region considered according to the procedure in M25.

We present the profiles of electron density and temperature from Chandra and XMM in Fig 5. The Chandra data are able to more finely resolve the center of the cluster, as demonstrated by the sharply peaked density and the identification of the cool core. Beyond the central XMM bin, where the impact of the larger PSF was substantial, we saw very good agreement in the radial density profiles. Using these profiles, we also computed the X-ray Pseudo-Entropy ( $K = k_B T_X \times n_e^{-2/3}$ ) and cooling time

$$t_{\text{cool}} = \frac{3}{2} \frac{(n_e + n_p) k T}{n_e n_p \Lambda(T, Z)}, \quad (1)$$

where  $\Lambda(T, Z)$  is the cooling function of the gas. Notably, the temperature of the gas in the inner 40kpc of the cluster was constrained to be  $1.8 \pm 0.6$  keV, with a corresponding central entropy of  $9 \pm 4$  keV cm<sup>2</sup> and cooling time of  $t_{\text{cool}} = 280_{-120}^{+150}$  Myr. Neither telescope could constrain more than a single, spatially-averaged, emission-weighted metallicity, with  $Z_{\text{XMM}} = 0.43_{-0.25}^{+0.46}$  and  $Z_{\text{Chandra}} = 0.31 \pm 0.25$ , respectively. Here, we have applied the cross-calibration factor of  $\ln(Z/Z^{\text{Cha}}) = 0.28_{-0.07}^{+0.10}$  to the Chandra metallicity from Flores et al. (2021) which provides better agreement between Chandra-measured abundances and those of Suzaku and XMM.

#### 4.4. Mass Estimates

We integrated the deprojected radial density profiles from Sec 4.3 and used them to simultaneously constrain  $r_{\Delta}$  and  $M_{\Delta}$  for  $\Delta = 2500$  and  $500$ , accounting for the correlated measurement uncertainties in density as a function of radius. When calculating total mass, we assumed fiducial  $f_{\text{gas}} = M_{\text{gas}}/M_{\text{tot}}$  values of  $0.113$  at  $r_{2500}$  and  $0.125$  at  $r_{500}$  based on measurements of similar clusters at  $z \leq 1.063$  (Allen et al. 2008; Mantz et al. 2016b). We note that the gas mass fraction at these overdensities is not expected to evolve significantly with redshift for large halos based on cosmological scale hydrodynamical simulations (e.g. Eke et al. 1998; Nagai et al. 2007; Battaglia et al. 2013; Planelles et al. 2013; Barnes et al. 2017; Singh et al. 2020; Rasia et al. 2025; Aljamal et al. 2025). For ACT-CL 0123, we measured  $r_{2500} = 206 \pm 14$ kpc ( $\sim 25''$ ) with an enclosed mass of  $M_{2500} = 6.7 \pm 1.3 \times 10^{13} M_{\odot}$ . Only by using the XMM data could we reach radii larger than  $r > r_{500}$ , yielding  $r_{500} = 590 \pm 40$ kpc ( $\sim 70''$ ) and  $M_{500} = 3.1 \pm 0.6 \times 10^{14} M_{\odot}$ .

#### 4.5. BCG Photometric Modeling

ACT-CL J0123 lacks any detailed spectroscopic optical/near-IR follow-up of its galaxy population. In lieu of this, we combined optical photometry of the cluster BCG in the  $g, r, i, z$  bands from DR10 of the Legacy Survey (DECaLS; Dey et al. 2019) with  $W_1, W_2$  near-IR measurements from the CatWISE (AllWISE + NEOWISE; Eisenhardt et al. 2020) catalog constructed using observations from the Wide Field Infrared Explorer (WISE). We used the EXTINCTION package (Barbary 2016) to correct for local extinction/reddening given by the Cardelli et al. (1989) Milky Way model, fixed to the local value of  $A_V = 0.0869$  (Schlafly & Finkbeiner 2011). Using the PROSPECTOR code (Johnson et al. 2021), we fit these 6 corrected photometric points using a Simple Stellar Population model (SSP; Conroy et al. 2009; Conroy & Gunn 2010) to simultaneously constrain the total formed stellar mass, metallicity, and age of the BCG, with an additional free parameter to account for intrinsic dust extinction following the Kriek & Conroy (2013) attenuation curves. In these fits, we assumed the initial mass function (IMF) from Kroupa (2001). We obtained posterior distributions for these parameters by running MCMC chains using the EMCEE package (Foreman-Mackey et al. 2013). The resulting spectrum is plotted in Fig 6. Our photometric analysis of the BCG yielded a stellar metallicity of  $\log_{10}(Z/Z_{\odot}) = -0.19_{-0.28}^{+0.14}$ , a total formed stellar mass of  $M_* = 8.6_{-1.3}^{+2.3} \times 10^{11} M_{\odot}$ , and a galactic age of  $t_{\text{age}} = 1.5_{-0.9}^{+0.4}$  Gyr. The corresponding “surviving” galactic stellar mass (i.e. the galactic stellar mass at the time of observation) was found to be  $M_* = 4.9_{-0.9}^{+1.6} \times 10^{11} M_{\odot}$ . Dust attenuation (defined as opacity at 5500Å) was constrained to be  $0.11_{-0.10}^{+0.13}$ . In addition to this choice of model, we tested models neglecting intrinsic dust extinction (i.e. fixing opacity to 0) and found strong statistical evidence that dust should be included as a free parameter. We also tested whether a delayed star formation model is preferred to an instantaneous starburst, but found no statistical preference for this more complex model (whether dust was included or not) and no significant differences in the posteriors of common fitted parameters. These data suggest that there has been no significant star formation in the BCG for the past  $\sim 1.5$  Gyr (when the Universe was  $\sim 2.7$  Gyr old), with the bulk of the stellar mass formed at a redshift of  $2.4_{-0.6}^{+0.4}$ .

## 5. DISCUSSION

Based on the imaging and spectroscopic results outlined here, ACT-CL J0123 is the highest-redshift dynamically relaxed, cool core cluster discovered to date. The SPA morphological tests in this work were depen-

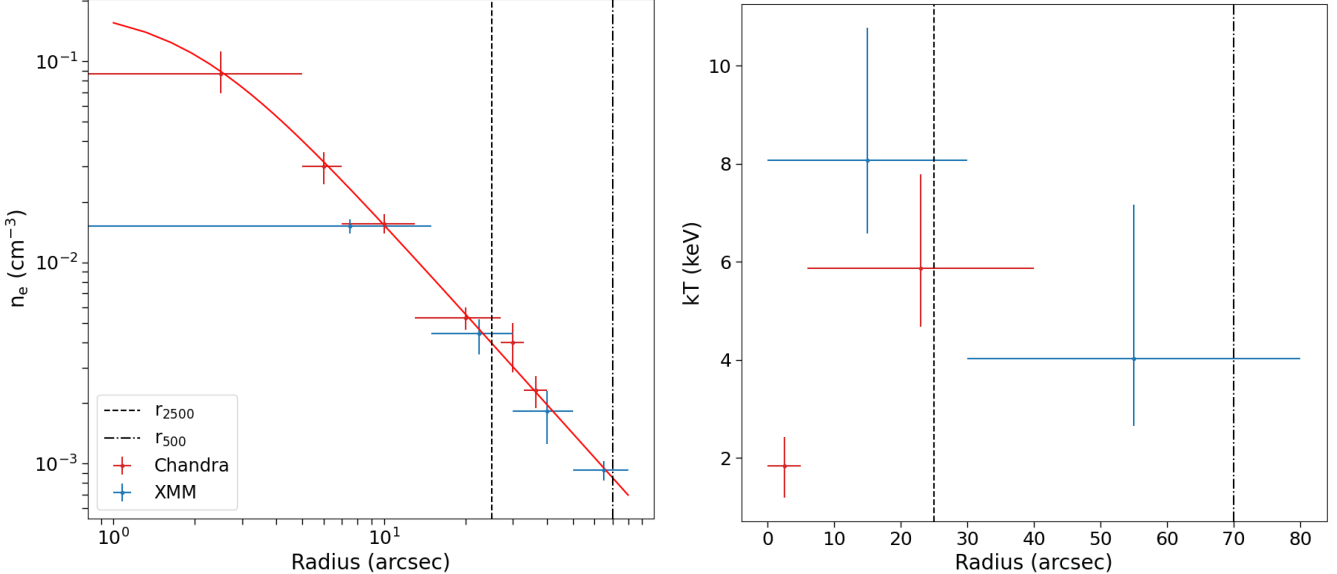


**Figure 5.** Density (left) and temperature (right) profiles for ACT-CL J0123 as measured by Chandra (red) and XMM (blue). Chandra is able to resolve more of the inner density profile, demonstrating its peakiness, and identifies the cool core. A  $\beta$ -model fit to the Chandra density (solid red curve) shows good agreement with XMM beyond the central bin, even at large radii where Chandra cannot probe.

dent on the Chandra data, as XMM-Newton could not adequately probe the cluster core with its poorer spatial resolution. In principle, XMM data could help characterize ICM dynamics of high-redshift clusters at more intermediate radii (see Bartalucci et al. 2017), but in this case this would be complicated by the nearby point source (Fig 2) and the diminished azimuthal coverage and statistics as a result of the required masking.

Despite the ICM reaching low entropies in the core, a feature often associated with star formation in the BCGs of cool core clusters (Cavagnolo et al. 2008; Voit et al. 2008; Calzadilla et al. 2024), we saw no evidence for ongoing or recent star formation in the BCG of ACT-CL J0123 based on currently available optical/near-IR photometry (Sec 4.5). In contrast, the BCG of the next highest redshift relaxed cluster, SPT-CL J2215–3537 ( $z = 1.16$ ; Calzadilla et al. 2023), exhibits a starburst of  $> 300 \text{ M}_\odot \text{ yr}^{-1}$ . However, not all high-redshift relaxed systems demonstrate high levels of star formation. At slightly lower redshift ( $z = 1.02$ ), the central galaxy of relaxed cluster WARP J1415.1+3612 also exhibits a low core entropy ( $9.9 \pm 2.0 \text{ keV cm}^2$ ), with an upper limit on the star formation rate of its BCG of  $< 10 \text{ M}_\odot \text{ yr}^{-1}$  (two orders of magnitude lower than predicted by the cooling rate; Santos et al. 2012). At  $z = 1.40$ , SPT-CL J0607–4448 is another example of a system with a comparatively high central gas density (and relatively low central entropy) for which a tight limit on the star

formation rate in its BCG of only  $\sim 1 \text{ M}_\odot \text{ yr}^{-1}$  has been obtained (Masterson et al. 2023).<sup>21</sup>

The canonical explanation for quenched star formation in cool core galaxy clusters is AGN feedback, which provides heat to offset runaway cooling. It is possible for the central galaxy of relaxed, high redshift clusters to be remarkably active; at  $z = 1.06$ , 3C 186 represents an extreme example, where the BCG is an exceptionally bright radio-loud quasar (Siemiginowska et al. 2010). However, for ACT-CL J0123, the current non-detection of a central X-ray point source and lack of AGN signatures in the IR (CatWISE) and existing radio data (VLASS) argue against such a possibility. We do note a slight deficit of counts to the SW of the cluster center in the native-resolution Chandra image, which may be indicative of recent jet-ICM interactions (Fig 2); however, the existing data are insufficient to further explore the possibility of cavities in the intracluster gas at present.

Our photometric analysis of the BCG suggests that there has been no significant star formation in the BCG for the past  $\sim 1.5$  Gyr. However, we note that the existing data are somewhat limiting. Currently, the only photometry redward of the 4000Å break come from WISE, whose large PSF ( $\sim 6''$  in  $W_1$  and  $W_2$ ) could result in significant blending. This issue is mitigated some-

<sup>21</sup> However, SPT-CL J0607–4448 does not exhibit a cool core with a central temperature drop in its central 50 kpc, nor is surface brightness “peaky” enough for the cluster to meet the SPA criteria for dynamical relaxation.

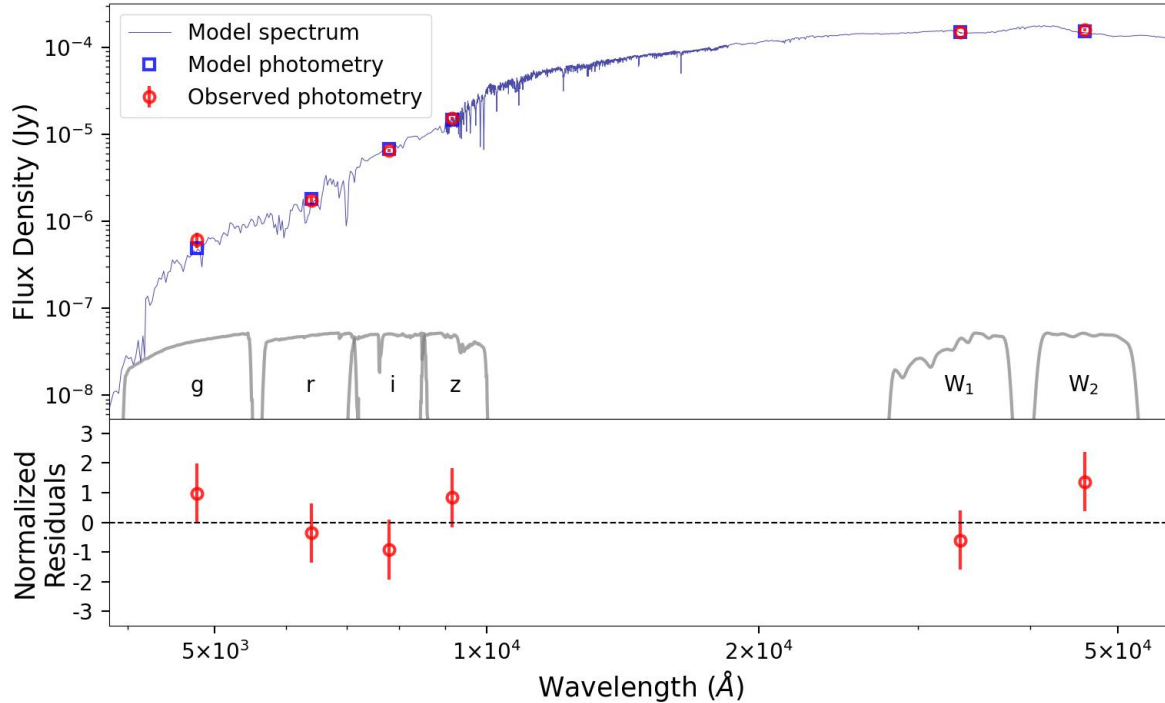


**Figure 6.** *Top:* Best fitting simple stellar population (i.e. starburst) model spectrum to observed-frame optical (DECaLS  $g, r, i, z$ ) and near-IR (WISE  $W_1$  and  $W_2$ ) photometry for the BCG of ACT-CL J0123. The photometric data with error bars are plotted in red. The relative transmission curves for each photometric band are plotted in gray and labeled by name. Using a simple stellar population model (SSP) in PROSPECTOR, we obtain the best-fitting SED and corresponding model photometry (blue curve and squares, respectively). *Bottom:* Normalized residuals for the best fit SSP model. This spectrum points toward the BCG hosting an evolved stellar population, with no evidence for active star formation for more than a Gyr before the time of observation.

what by the forced photometry employed for the DECaLS catalogues (Dey et al. 2019), but these fits would be significantly enhanced by additional near-IR imaging or spectroscopy at higher spatial resolution (e.g. from JWST). In our fits, we see significant degeneracy between dust attenuation and the age of the last starburst, with higher opacity corresponding to a more recent starburst. Free intrinsic extinction is greatly statistically preferred; however, simply including this free parameter reduces the best-fit stellar age by  $\sim 1$  Gyr. To place the best constraints on the stellar history of this BCG (and that of other cluster members), photometry bridging the DECaLS and WISE observations would be particularly useful.

Observations of high redshift galaxy clusters are also invaluable to explore the history of cosmic enrichment. As the available XMM data only provided a bulk detection of metallicity within the cluster of  $Z/Z_{\odot} = 0.43^{+0.46}_{-0.25}$ , we currently are unable to comment on the radial abundance distribution in the ICM. However, high redshift studies of cluster metallicity would lead us to expect the Fe abundance to drop to  $0.2 \lesssim Z/Z_{\odot} \lesssim 0.3$  by

$r_{500}$  (Ettori et al. 2015; McDonald et al. 2016; Mantz et al. 2017; Liu et al. 2020; Flores et al. 2021), and it would be interesting to determine whether ACT-CL J0123 hosts a metallicity gradient. Central metallicity gradients present at the time of cluster formation can remain in place without merger activity (or significant AGN outbursts) to distribute metals to larger radii, as seen in a variety of observations (e.g. Allen & Fabian 1998; De Grandi & Molendi 2001) and simulations (e.g. Rasia et al. 2015). Moreover, the cores (on  $\sim 10$  kpc scales) of highly relaxed systems can reveal near-Solar metallicities (McDonald et al. 2019) or even more extreme abundances, such as the  $\sim 3Z_{\odot}$  core seen in WARP J1415.1+3612 (Santos et al. 2012). Even for other high- $z$  relaxed clusters where the central metallicity is not as extreme (e.g. SPT-CL J0615–5746 and SPT-CL J2215–3537), core and core-excised metallicity ratios of  $\sim 2$  are still observed (Jiménez-Teja et al. 2023; Stueber et al. 2026).

The observed thermodynamic properties of clusters as a function of redshift also provide a powerful probe of cluster evolution. In the context of the self-similar model

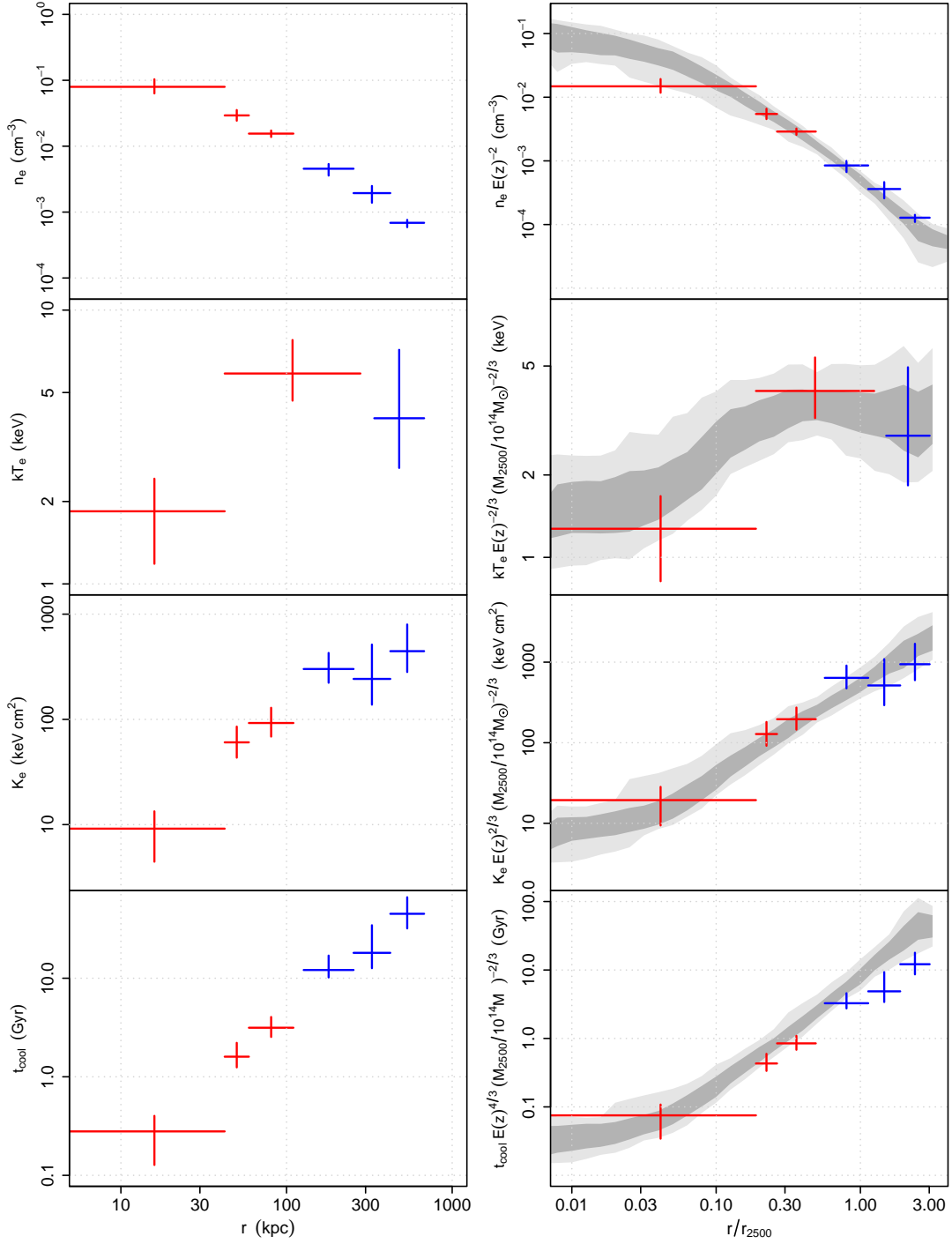


**Figure 7.** Thermodynamic profiles for ICM electron density, temperature, pseudoentropy, and cooling time (top → bottom) of relaxed clusters. ACT-CL J0123 is constrained at small radii by Chandra (red points) and at large radii by XMM-Newton (blue points). Profiles of ACT-CL J0123 alone are presented on the left, unscaled, with the radius in physical units. Profiles on the right include self-similar scaling factors, and are compared with an ensemble of 40 relaxed systems (grey band) previously analyzed in Mantz et al. (2016b).

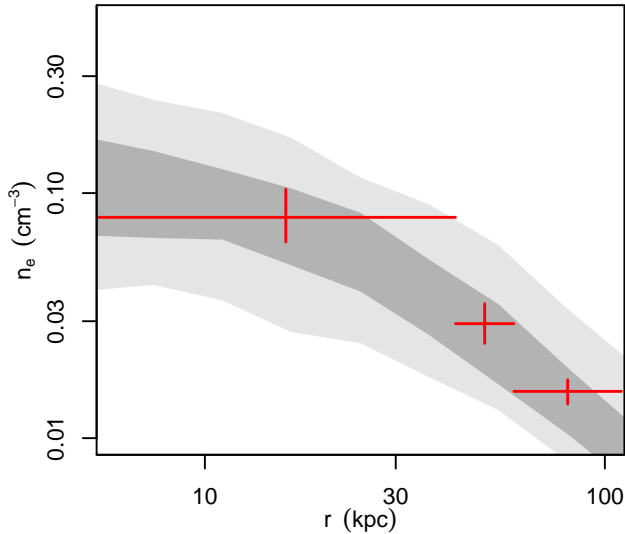


**Figure 8.** Central ICM density profile of ACT-CL J0123 compared to the sample of relaxed clusters from Mantz et al. (2016b), without self-similar scaling (c.f. Fig 7).

(Kaiser 1986), where galaxy clusters form purely from gravitational collapse, the observable properties of clusters (density, thermodynamics, luminosity, etc), should scale simply with redshift and mass. Hydrodynamical simulations have also been used to study the evolution of clusters, incorporating additional astrophysical processes including cooling and feedback from stars and AGN (for a review, see Borgani & Kravtsov 2011). More recent work (including e.g. MACSIS, Millennium, ILLUSTRIS-TNG, TNG-CLUSTER, and FLAMINGO; Battaglia et al. 2012; Kay et al. 2012; Barnes et al. 2017; Pop et al. 2022; Aljamal et al. 2025) shows that, even in the presence of feedback processes, scaling relations for the most massive halos (with  $M_{500} \gtrsim 10^{14} M_{\odot}$ ) should follow self-similar predictions quite closely at intermediate to large scales. Only in the centers of such clusters, and particularly cool core systems, are deviations from self-similar predictions routinely observed (Arnaud et al. 2010; McDonald et al. 2014; Mantz et al. 2016b; McDonald et al. 2019).

ACT-CL J0123 follows this general picture well. Figure 7, Figure 8, and Figure 9 each show a comparison of the properties of ACT-CL J0123 against those of the relaxed galaxy cluster sample of (Mantz et al. 2016b), spanning the redshift range  $0 \lesssim z \lesssim 1.063$ . Fig 7 presents the radial profiles of ICM electron density, temperature, pseudo-entropy, and cooling time both unscaled and scaled self similarly. For these profiles, the ACT-CL J0123 measurements from Chandra and XMM have been combined, using Chandra for the inner 100 kpc where we require high spatial resolution to resolve

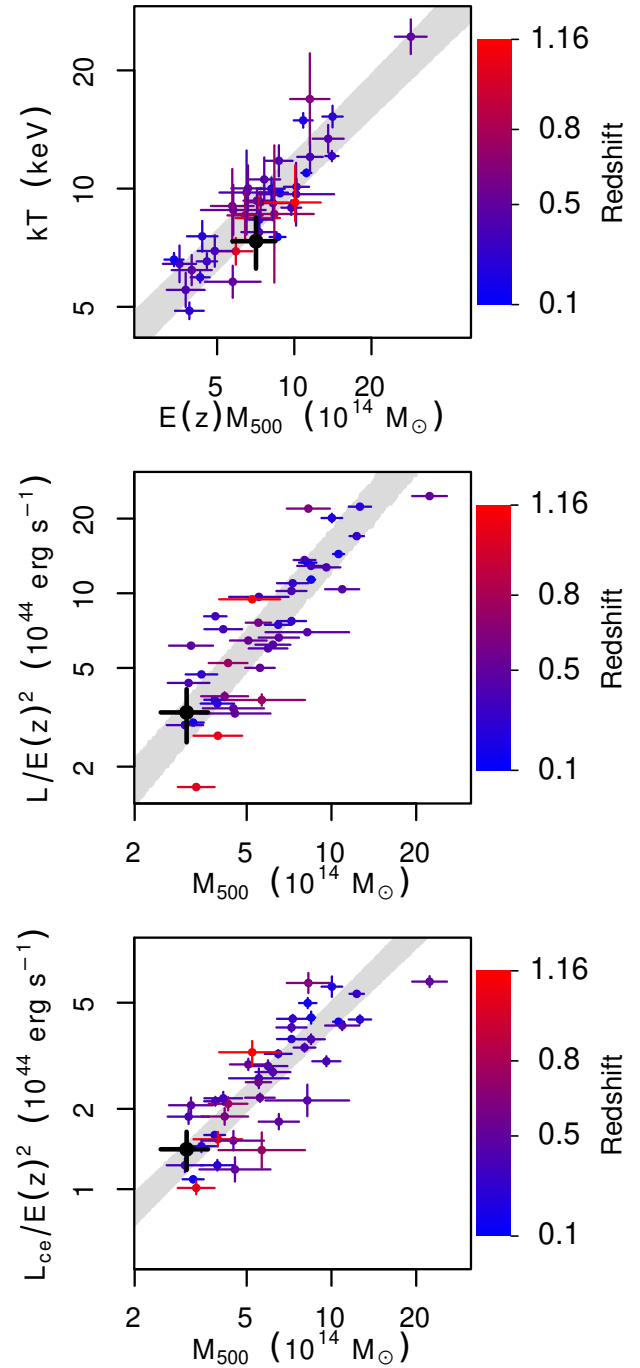


**Figure 9.** Mass, temperature, luminosity, and core-excised luminosity of ACT-CL J0123 compared to that of the relaxed cluster samples from Mantz et al. (2016b). Clusters are colored in order of increasing redshift (blue  $\rightarrow$  red), with ACT-CL J0123 in black. The grey shading is the  $1\sigma$  predictive range (including intrinsic scatter) surrounding a best fit powerlaw to the data in Mantz et al. (2016b) out to  $z = 1.06$ . The reddest point (SPT-CL J2215-3537 at  $z = 1.16$ ; Stueber et al. 2026) is not included in this fit. ACT-CL J0123 is consistent with the existing scaling relations.

$z_{\text{spec}}$	$r_{500}$ (kpc)	$M_{500}$ ( $10^{14} M_{\odot}$ )	$M_{\text{gas}}$ ( $10^{13} M_{\odot}$ )	$kT$ (keV)	$L_{0.1-2.4}$ ( $10^{45} \text{ ergs s}^{-1}$ )	$Z$ (Solar)
$1.50 \pm 0.03$	$590 \pm 40$	$3.1 \pm 0.6$	$3.8 \pm 0.7$	$7.3 \pm 1.1$	$1.8 \pm 0.4$	$0.43^{+0.46}_{-0.25}$

**Table 1.** Global properties of ACT-CL J0123. A redshift of  $z = 1.5$  has been assumed in the calculation of each property. Gas mass and  $r_{500}$  (and consequently  $M_{500}$ ) are simultaneously constrained using the 3-D deprojected radial profiles (Sections 4.3/4.4), while luminosity has been calculated in projection within  $r_{500}$ .

the cool core, and XMM for the remaining bins where we lack the statistics from Chandra to make precise measurements. The scaled measurements agree well with the full relaxed sample at large radius, providing evidence for self-similar evolution at intermediate-to-large radii in the dynamically relaxed cluster population out to  $z = 1.5$ . We note, however, that the scaled density of the innermost bin is lower than the mean profile. Fig 8 presents the central density of ACT-CL J0123 compared to the relaxed sample without scaling, where we find better agreement. This result extends the findings of McDonald et al. (2017) which suggests that the physical state of the centers of cool core clusters are maintained to be approximately constant by AGN feedback since high redshift.

Figure 9 presents the mass, temperature, and luminosity of ACT-CL J0123 compared to the galaxy cluster scaling relations measured in Mantz et al. (2016b) in addition to the relaxed cluster SPT-CL J2215–3537 at  $z = 1.16$  (Stueber et al. 2026). Because ACT-CL J0123 does not have deep enough data to constrain its mass directly, the value of  $M_{500}$  reported here is the gas mass  $M_{\text{gas}}$  divided by the fiducial value of  $f_{\text{gas}} = 0.125$  at  $r_{500}$  (Mantz et al. 2016b). Luminosity is calculated in the 0.1–2.4 keV band, and we report both the total luminosity of the cluster, as well as the center-excised luminosity. The center-excised luminosity,  $L_{\text{ce}}$ , excludes radii  $r < 0.15r_{500}$  in projection, and typically provides a lower-scatter mass proxy (bottom panel of Fig 9; see Mantz et al. 2016b, 2018 for further details). Measurements of the temperature similarly excluded constraints from the central radii where the cool core would have a strong effect, though this measurement comes solely from XMM, which does not resolve the central drop in temperature in any case. As with  $M_{500}$  (Section 4.4), the uncertainty on these integrated quantities incorporates the uncertainty on  $r_{500}$  itself. Overall, ACT-CL J0123 is highly consistent with the existing population of relaxed clusters and supports previous suggestions that the bulk of clusters generally evolve self-similarly with the exception of the inner density profiles of relaxed/cool core systems. These global properties are reported in Table 1

## 6. SUMMARY AND CONCLUSIONS

We report the identification of ACT-CL J0123.5–0428 as the highest-redshift dynamically relaxed, cool core

galaxy cluster discovered to date. Our primary findings can be summarized as follows:

- Our Chandra X-ray imaging analysis of ACT-CL J0123.5–0428 shows it to be morphologically relaxed according to the SPA criteria of Mantz et al. (2015), with symmetry, peakiness, and alignment metrics of  $s = 1.3 \pm 0.2$ ,  $p = -0.7 \pm 0.2$ , and  $a = 1.3 \pm 0.2$ , respectively.
- An XMM spectral analysis provides the first spectroscopic confirmation of ACT-CL J0123 at  $z = 1.50 \pm 0.03$ , making it the highest redshift dynamically relaxed cool core cluster identified to date, providing a substantial increase in redshift compared to the existing samples of relaxed systems ( $z \leq 1.16$ ; Mantz et al. 2022).
- The Chandra and XMM data confirm ACT-CL J0123 to be one of the hottest ( $kT = 7.3 \pm 1.1$  keV), most X-ray luminous ( $L_{\text{X}} = 1.8 \pm 0.4 \times 10^{45}$  ergs/s) and massive clusters ( $M_{500} = 3.1 \pm 0.6 \times 10^{14} M_{\odot}$ ) known at high redshifts.
- A Chandra spectral analysis of the inner 40 kpc of this system reveals a strong cool core ( $1.8 \pm 0.6$  keV) with a low cooling time ( $t_{\text{cool}} = 280^{+150}_{-120}$  Myr).
- A deprojected spectral analysis of the Chandra and XMM data is able to jointly resolve ICM thermodynamic properties both within  $r_{2500}$  and out to  $r_{500}$ . The mean, emission-weighted ICM metallicity is constrained to be  $Z/Z_{\odot} = 0.43^{+0.46}_{-0.25}$ .
- Comparison of the observed properties of ACT-CL J0123 to an existing sample of relaxed clusters (Mantz et al. 2016b) provides further evidence that clusters evolve self-similarly at large scales, while the inner ICM densities of cool core clusters remain roughly constant across cosmic time.
- A photometric analysis of the BCG of ACT-CL J0123 reveals an evolved stellar population with no evidence for recent star formation. The data are consistent with an instantaneous starburst that occurred  $\sim 2.3$ – $3.5$  Gyr after the Big Bang.

ACT-CL J0123.5–0428 is a prime example of why both high spatial resolution and high sensitivity are needed for the study of relaxed clusters at high redshift. With deeper data, further work could be done to better resolve the structure of the cool core and the distribution of metallicity within the cluster as a whole. At this time, supplemental XMM data will be essentially required for the most complete studies of high-redshift clusters, as Chandra’s soft sensitivity continues to decrease and observations of this type become even more expensive to obtain. Accordingly, we highlight this study as a pathfinder for the next generation of X-ray missions, where instruments with high spatial resolution and high sensitivity (e.g. AXIS and NewAthena) will complement each other to continue this work at  $z > 1.5$ .

#### ACKNOWLEDGEMENTS

AMF is supported by the Future Investigators in NASA Earth and Space Science and Technology (FINESST) Program under award number 80NSSC23K1484. Support for this work was provided in part by the National Aeronautics and Space Administration through Chandra Award Number GO3-24111A issued by the Chandra X-ray Center, which is operated by the Smithso-

nian Astrophysical Observatory for and on behalf of the National Aeronautics Space Administration under contract NAS8-03060. Work supported in part by the U.S. Department of Energy under contract number DE-AC02-76SF00515. This research has made use of data obtained from the Chandra Data Archive provided by the Chandra X-ray Center (CXC) in addition to observations obtained with XMM-Newton, an ESA science mission with instruments and contributions directly funded by ESA Member States and NASA.

#### Facilities: CXO, XMM

*Software:* ACX (Smith et al. 2012, 2014; <http://atomdb.org/CX>), Astropy (Greenfield et al. 2013; Astropy Collaboration et al. 2013, 2018, 2022), CIAO (Fruscione et al. 2006; CIAO Development Team 2013), ESAS (<https://heasarc.gsfc.nasa.gov/docs/xmm/esas>), HEASOFT (NASA High Energy Astrophysics Science Archive Research Center (Heasarc) 2014), LMC (Mantz 2017), MARX (Davis et al. 2012; Wise et al. 2013), SAS (SAS development team 2014), SXRBG (Sabol & Snowden 2019), XSPEC (Arnaud 1996; Arnaud et al. 1999), Prospector (Johnson et al. 2021), extinction (Barbary 2016)

#### REFERENCES

Aljamal, E., Evrard, A. E., Farahi, A., et al. 2025, MNRAS, 544, 67, doi: [10.1093/mnras/staf1665](https://doi.org/10.1093/mnras/staf1665)

Allen, S. W. 2000, MNRAS, 315, 269, doi: [10.1046/j.1365-8711.2000.03395.x](https://doi.org/10.1046/j.1365-8711.2000.03395.x)

Allen, S. W., Evrard, A. E., & Mantz, A. B. 2011, ARA&A, 49, 409, doi: [10.1146/annurev-astro-081710-102514](https://doi.org/10.1146/annurev-astro-081710-102514)

Allen, S. W., & Fabian, A. C. 1998, MNRAS, 297, L63, doi: [10.1046/j.1365-8711.1998.01738.x](https://doi.org/10.1046/j.1365-8711.1998.01738.x)

Allen, S. W., & Mantz, A. B. 2019, in The Chandra X-ray Observatory, ed. B. Wilkes & W. Tucker, 10–1, doi: [10.1088/2514-3433/ab43dcch10](https://doi.org/10.1088/2514-3433/ab43dcch10)

Allen, S. W., Rapetti, D. A., Schmidt, R. W., et al. 2008, MNRAS, 383, 879, doi: [10.1111/j.1365-2966.2007.12610.x](https://doi.org/10.1111/j.1365-2966.2007.12610.x)

Allen, S. W., Schmidt, R. W., Ebeling, H., Fabian, A. C., & van Speybroeck, L. 2004, MNRAS, 353, 457, doi: [10.1111/j.1365-2966.2004.08080.x](https://doi.org/10.1111/j.1365-2966.2004.08080.x)

Allen, S. W., Schmidt, R. W., & Fabian, A. C. 2002, MNRAS, 334, L11, doi: [10.1046/j.1365-8711.2002.05601.x](https://doi.org/10.1046/j.1365-8711.2002.05601.x)

Amodeo, S., Ettori, S., Capasso, R., & Sereno, M. 2016, A&A, 590, A126, doi: [10.1051/0004-6361/201527630](https://doi.org/10.1051/0004-6361/201527630)

Arnaud, K., Dorman, B., & Gordon, C. 1999, XSPEC: An X-ray spectral fitting package, Astrophysics Source Code Library, record ascl:9910.005

Arnaud, K. A. 1996, in Astronomical Society of the Pacific Conference Series, Vol. 101, Astronomical Data Analysis Software and Systems V, ed. G. H. Jacoby & J. Barnes, 17

Arnaud, M., Pratt, G. W., Piffaretti, R., et al. 2010, A&A, 517, A92, doi: [10.1051/0004-6361/200913416](https://doi.org/10.1051/0004-6361/200913416)

Asplund, M., Grevesse, N., Sauval, A. J., & Scott, P. 2009, ARA&A, 47, 481, doi: [10.1146/annurev.astro.46.060407.145222](https://doi.org/10.1146/annurev.astro.46.060407.145222)

Astropy Collaboration, Robitaille, T. P., Tollerud, E. J., et al. 2013, A&A, 558, A33, doi: [10.1051/0004-6361/201322068](https://doi.org/10.1051/0004-6361/201322068)

Astropy Collaboration, Price-Whelan, A. M., Sipőcz, B. M., et al. 2018, AJ, 156, 123, doi: [10.3847/1538-3881/aabc4f](https://doi.org/10.3847/1538-3881/aabc4f)

Astropy Collaboration, Price-Whelan, A. M., Lim, P. L., et al. 2022, ApJ, 935, 167, doi: [10.3847/1538-4357/ac7c74](https://doi.org/10.3847/1538-4357/ac7c74)

Balucinska-Church, M., & McCammon, D. 1992, ApJ, 400, 699, doi: [10.1086/172032](https://doi.org/10.1086/172032)

Barbary, K. 2016, extinction v0.3.0, Zenodo, doi: [10.5281/zenodo.804967](https://doi.org/10.5281/zenodo.804967)

Barnes, D. J., Kay, S. T., Henson, M. A., et al. 2017, MNRAS, 465, 213, doi: [10.1093/mnras/stw2722](https://doi.org/10.1093/mnras/stw2722)

Bartalucci, I., Arnaud, M., Pratt, G. W., et al. 2017, *A&A*, 598, A61, doi: [10.1051/0004-6361/201629509](https://doi.org/10.1051/0004-6361/201629509)

Battaglia, N., Bond, J. R., Pfrommer, C., & Sievers, J. L. 2012, *ApJ*, 758, 74, doi: [10.1088/0004-637X/758/2/74](https://doi.org/10.1088/0004-637X/758/2/74)

—. 2013, *ApJ*, 777, 123, doi: [10.1088/0004-637X/777/2/123](https://doi.org/10.1088/0004-637X/777/2/123)

Bleem, L. E., Stalder, B., de Haan, T., et al. 2015, *ApJS*, 216, 27, doi: [10.1088/0067-0049/216/2/27](https://doi.org/10.1088/0067-0049/216/2/27)

Bleem, L. E., Bocquet, S., Stalder, B., et al. 2020, *ApJS*, 247, 25, doi: [10.3847/1538-4365/ab6993](https://doi.org/10.3847/1538-4365/ab6993)

Böhringer, H., & Werner, N. 2010, *A&A Rv*, 18, 127, doi: [10.1007/s00159-009-0023-3](https://doi.org/10.1007/s00159-009-0023-3)

Bonamente, M., Joy, M. K., LaRoque, S. J., et al. 2006, *ApJ*, 647, 25, doi: [10.1086/505291](https://doi.org/10.1086/505291)

Borgani, S., & Kravtsov, A. 2011, *Advanced Science Letters*, 4, 204. <https://arxiv.org/abs/0906.4370>

Calzadilla, M. S., Bleem, L. E., McDonald, M., et al. 2023, *ApJ*, 947, 44, doi: [10.3847/1538-4357/acc6c2](https://doi.org/10.3847/1538-4357/acc6c2)

Calzadilla, M. S., McDonald, M., Benson, B. A., et al. 2024, *ApJ*, 976, 169, doi: [10.3847/1538-4357/ad8916](https://doi.org/10.3847/1538-4357/ad8916)

Cardelli, J. A., Clayton, G. C., & Mathis, J. S. 1989, *ApJ*, 345, 245, doi: [10.1086/167900](https://doi.org/10.1086/167900)

Cash, W. 1979, *ApJ*, 228, 939, doi: [10.1086/156922](https://doi.org/10.1086/156922)

Cavagnolo, K. W., Donahue, M., Voit, G. M., & Sun, M. 2008, *ApJL*, 683, L107, doi: [10.1086/591665](https://doi.org/10.1086/591665)

CIAO Development Team. 2013, CIAO: Chandra Interactive Analysis of Observations, *Astrophysics Source Code Library*, record ascl:1311.006

Conroy, C., & Gunn, J. E. 2010, *ApJ*, 712, 833, doi: [10.1088/0004-637X/712/2/833](https://doi.org/10.1088/0004-637X/712/2/833)

Conroy, C., Gunn, J. E., & White, M. 2009, *ApJ*, 699, 486, doi: [10.1088/0004-637X/699/1/486](https://doi.org/10.1088/0004-637X/699/1/486)

Crawford, C. S., Allen, S. W., Ebeling, H., Edge, A. C., & Fabian, A. C. 1999, *MNRAS*, 306, 857, doi: [10.1046/j.1365-8711.1999.02583.x](https://doi.org/10.1046/j.1365-8711.1999.02583.x)

Darragh-Ford, E., Mantz, A. B., Rasia, E., et al. 2023, *MNRAS*, 521, 790, doi: [10.1093/mnras/stad585](https://doi.org/10.1093/mnras/stad585)

Davis, J. E., Bautz, M. W., Dewey, D., et al. 2012, in *Society of Photo-Optical Instrumentation Engineers (SPIE) Conference Series*, Vol. 8443, *Space Telescopes and Instrumentation 2012: Ultraviolet to Gamma Ray*, ed. T. Takahashi, S. S. Murray, & J.-W. A. den Herder, 84431A, doi: [10.1117/12.926937](https://doi.org/10.1117/12.926937)

De Grandi, S., & Molendi, S. 2001, *ApJ*, 551, 153, doi: [10.1086/320098](https://doi.org/10.1086/320098)

Dey, A., Schlegel, D. J., Lang, D., et al. 2019, *AJ*, 157, 168, doi: [10.3847/1538-3881/ab089d](https://doi.org/10.3847/1538-3881/ab089d)

Donahue, M., Bruch, S., Wang, E., et al. 2010, *ApJ*, 715, 881, doi: [10.1088/0004-637X/715/2/881](https://doi.org/10.1088/0004-637X/715/2/881)

Edge, A. C. 2001, *MNRAS*, 328, 762, doi: [10.1046/j.1365-8711.2001.04802.x](https://doi.org/10.1046/j.1365-8711.2001.04802.x)

Edge, A. C., Oonk, J. B. R., Mittal, R., et al. 2010, *A&A*, 518, L46, doi: [10.1051/0004-6361/201014569](https://doi.org/10.1051/0004-6361/201014569)

Ehler, K., Weinberger, R., Pfrommer, C., Pakmor, R., & Springel, V. 2023, *MNRAS*, 518, 4622, doi: [10.1093/mnras/stac2860](https://doi.org/10.1093/mnras/stac2860)

Eisenhardt, P. R. M., Marocco, F., Fowler, J. W., et al. 2020, *ApJS*, 247, 69, doi: [10.3847/1538-4365/ab7f2a](https://doi.org/10.3847/1538-4365/ab7f2a)

Eke, V. R., Navarro, J. F., & Frenk, C. S. 1998, *ApJ*, 503, 569, doi: [10.1086/306008](https://doi.org/10.1086/306008)

Ettori, S., Baldi, A., Balestra, I., et al. 2015, *A&A*, 578, A46, doi: [10.1051/0004-6361/201425470](https://doi.org/10.1051/0004-6361/201425470)

Ettori, S., Morandi, A., Tozzi, P., et al. 2009, *A&A*, 501, 61, doi: [10.1051/0004-6361/200810878](https://doi.org/10.1051/0004-6361/200810878)

Fabian, A. C. 1994, *ARA&A*, 32, 277, doi: [10.1146/annurev.aa.32.090194.001425](https://doi.org/10.1146/annurev.aa.32.090194.001425)

—. 2012, *ARA&A*, 50, 455, doi: [10.1146/annurev-astro-081811-125521](https://doi.org/10.1146/annurev-astro-081811-125521)

Fabian, A. C., Hu, E. M., Cowie, L. L., & Grindlay, J. 1981, *ApJ*, 248, 47, doi: [10.1086/159128](https://doi.org/10.1086/159128)

Flores, A. M., Mantz, A. B., Allen, S. W., et al. 2021, *MNRAS*, 507, 5195, doi: [10.1093/mnras/stab2430](https://doi.org/10.1093/mnras/stab2430)

Foreman-Mackey, D., Hogg, D. W., Lang, D., & Goodman, J. 2013, *PASP*, 125, 306, doi: [10.1086/670067](https://doi.org/10.1086/670067)

Fruscione, A., McDowell, J. C., Allen, G. E., et al. 2006, in *Society of Photo-Optical Instrumentation Engineers (SPIE) Conference Series*, Vol. 6270, *Observatory Operations: Strategies, Processes, and Systems*, ed. D. R. Silva & R. E. Doxsey, 62701V, doi: [10.1117/12.671760](https://doi.org/10.1117/12.671760)

Greenfield, P., Robitaille, T., Tollerud, E., et al. 2013, *Astropy: Community Python library for astronomy, Astrophysics Source Code Library*, record ascl:1304.002

HI4PI Collaboration, Ben Bekhti, N., Flöer, L., et al. 2016, *A&A*, 594, A116, doi: [10.1051/0004-6361/201629178](https://doi.org/10.1051/0004-6361/201629178)

Hilton, M., Sifón, C., Naess, S., et al. 2021, *ApJS*, 253, 3, doi: [10.3847/1538-4365/abd023](https://doi.org/10.3847/1538-4365/abd023)

Hlavacek-Larrondo, J., McDonald, M., Benson, B. A., et al. 2015, *ApJ*, 805, 35, doi: [10.1088/0004-637X/805/1/35](https://doi.org/10.1088/0004-637X/805/1/35)

Huang, N., Bleem, L. E., Stalder, B., et al. 2020, *AJ*, 159, 110, doi: [10.3847/1538-3881/ab6a96](https://doi.org/10.3847/1538-3881/ab6a96)

Jiménez-Teja, Y., Dupke, R. A., Lopes, P. A. A., & Vilchez, J. M. 2023, *A&A*, 676, A39, doi: [10.1051/0004-6361/202346580](https://doi.org/10.1051/0004-6361/202346580)

Johnson, B. D., Leja, J., Conroy, C., & Speagle, J. S. 2021, *ApJS*, 254, 22, doi: [10.3847/1538-4365/abef67](https://doi.org/10.3847/1538-4365/abef67)

Kaiser, N. 1986, *MNRAS*, 222, 323

Kay, S. T., Peel, M. W., Short, C. J., et al. 2012, *MNRAS*, 422, 1999, doi: [10.1111/j.1365-2966.2012.20623.x](https://doi.org/10.1111/j.1365-2966.2012.20623.x)

Kozmányan, A., Bourdin, H., Mazzotta, P., Rasia, E., & Sereno, M. 2019, *A&A*, 621, A34, doi: [10.1051/0004-6361/201833879](https://doi.org/10.1051/0004-6361/201833879)

Kravtsov, A. V., & Borgani, S. 2012, *ARA&A*, 50, 353, doi: [10.1146/annurev-astro-081811-125502](https://doi.org/10.1146/annurev-astro-081811-125502)

Kriek, M., & Conroy, C. 2013, *ApJL*, 775, L16, doi: [10.1088/2041-8205/775/1/L16](https://doi.org/10.1088/2041-8205/775/1/L16)

Kriss, G. A., Cioffi, D. F., & Canizares, C. R. 1983, *ApJ*, 272, 439, doi: [10.1086/161311](https://doi.org/10.1086/161311)

Kroupa, P. 2001, *MNRAS*, 322, 231, doi: [10.1046/j.1365-8711.2001.04022.x](https://doi.org/10.1046/j.1365-8711.2001.04022.x)

Li, Y., Bryan, G. L., Ruszkowski, M., et al. 2015, *ApJ*, 811, 73, doi: [10.1088/0004-637X/811/2/73](https://doi.org/10.1088/0004-637X/811/2/73)

Li, Y., Ruszkowski, M., & Bryan, G. L. 2017, *ApJ*, 847, 106, doi: [10.3847/1538-4357/aa88c1](https://doi.org/10.3847/1538-4357/aa88c1)

Liu, A., Tozzi, P., Ettori, S., et al. 2020, *A&A*, 637, A58, doi: [10.1051/0004-6361/202037506](https://doi.org/10.1051/0004-6361/202037506)

Mantz, A. B. 2017, LMC: Logarithmantic Monte Carlo, *Astrophysics Source Code Library*, record ascl:1706.005

Mantz, A. B., Allen, S. W., & Morris, R. G. 2016a, *MNRAS*, 462, 681, doi: [10.1093/mnras/stw1707](https://doi.org/10.1093/mnras/stw1707)

Mantz, A. B., Allen, S. W., Morris, R. G., et al. 2020, *MNRAS*, 496, 1554, doi: [10.1093/mnras/staa1581](https://doi.org/10.1093/mnras/staa1581)

—. 2014, *MNRAS*, 440, 2077, doi: [10.1093/mnras/stu368](https://doi.org/10.1093/mnras/stu368)

Mantz, A. B., Allen, S. W., Morris, R. G., & Schmidt, R. W. 2016b, *MNRAS*, 456, 4020, doi: [10.1093/mnras/stv2899](https://doi.org/10.1093/mnras/stv2899)

Mantz, A. B., Allen, S. W., Morris, R. G., et al. 2015, *MNRAS*, 449, 199, doi: [10.1093/mnras/stv219](https://doi.org/10.1093/mnras/stv219)

—. 2017, *MNRAS*, 472, 2877, doi: [10.1093/mnras/stx2200](https://doi.org/10.1093/mnras/stx2200)

Mantz, A. B., Allen, S. W., Morris, R. G., & von der Linden, A. 2018, *MNRAS*, 473, 3072, doi: [10.1093/mnras/stx2554](https://doi.org/10.1093/mnras/stx2554)

Mantz, A. B., Flores, A. M., Somboonpanyakul, T., et al. 2025, *arXiv e-prints*, arXiv:2512.05405, doi: [10.48550/arXiv.2512.05405](https://doi.org/10.48550/arXiv.2512.05405)

Mantz, A. B., Morris, R. G., Allen, S. W., et al. 2022, *MNRAS*, 510, 131, doi: [10.1093/mnras/stab3390](https://doi.org/10.1093/mnras/stab3390)

Martz, C. G., McNamara, B. R., Nulsen, P. E. J., et al. 2020, *ApJ*, 897, 57, doi: [10.3847/1538-4357/ab96cd](https://doi.org/10.3847/1538-4357/ab96cd)

Masterson, M., McDonald, M., Ansarinejad, B., et al. 2023, *ApJ*, 944, 164, doi: [10.3847/1538-4357/acaе9е](https://doi.org/10.3847/1538-4357/acaе9е)

McDonald, M., Benson, B. A., Vikhlinin, A., et al. 2013, *ApJ*, 774, 23, doi: [10.1088/0004-637X/774/1/23](https://doi.org/10.1088/0004-637X/774/1/23)

—. 2014, *ApJ*, 794, 67, doi: [10.1088/0004-637X/794/1/67](https://doi.org/10.1088/0004-637X/794/1/67)

McDonald, M., McNamara, B. R., van Weeren, R. J., et al. 2015, *ApJ*, 811, 111, doi: [10.1088/0004-637X/811/2/111](https://doi.org/10.1088/0004-637X/811/2/111)

McDonald, M., Bulbul, E., de Haan, T., et al. 2016, *ApJ*, 826, 124, doi: [10.3847/0004-637X/826/2/124](https://doi.org/10.3847/0004-637X/826/2/124)

McDonald, M., Allen, S. W., Bayliss, M., et al. 2017, *ApJ*, 843, 28, doi: [10.3847/1538-4357/aa7740](https://doi.org/10.3847/1538-4357/aa7740)

McDonald, M., Allen, S. W., Hlavacek-Larrondo, J., et al. 2019, *ApJ*, 870, 85, doi: [10.3847/1538-4357/aaf394](https://doi.org/10.3847/1538-4357/aaf394)

McNamara, B. R., & Nulsen, P. E. J. 2007, *ARA&A*, 45, 117, doi: [10.1146/annurev.astro.45.051806.110625](https://doi.org/10.1146/annurev.astro.45.051806.110625)

—. 2012, *New Journal of Physics*, 14, 055023, doi: [10.1088/1367-2630/14/5/055023](https://doi.org/10.1088/1367-2630/14/5/055023)

Miyaji, T., Hasinger, G., Salvato, M., et al. 2015, *ApJ*, 804, 104, doi: [10.1088/0004-637X/804/2/104](https://doi.org/10.1088/0004-637X/804/2/104)

Nagai, D., Vikhlinin, A., & Kravtsov, A. V. 2007, *ApJ*, 655, 98, doi: [10.1086/509868](https://doi.org/10.1086/509868)

NASA High Energy Astrophysics Science Archive Research Center (Heasarc). 2014, HEAsoft: Unified Release of FTOOLS and XANADU, *Astrophysics Source Code Library*, record ascl:1408.004

O'Dea, C. P., Baum, S. A., Privon, G., et al. 2008, *ApJ*, 681, 1035, doi: [10.1086/588212](https://doi.org/10.1086/588212)

Olivares, V., Salome, P., Combes, F., et al. 2019, *A&A*, 631, A22, doi: [10.1051/0004-6361/201935350](https://doi.org/10.1051/0004-6361/201935350)

Peres, C. B., Fabian, A. C., Edge, A. C., et al. 1998, *MNRAS*, 298, 416, doi: [10.1046/j.1365-8711.1998.01624.x](https://doi.org/10.1046/j.1365-8711.1998.01624.x)

Planelles, S., Borgani, S., Dolag, K., et al. 2013, *MNRAS*, 431, 1487, doi: [10.1093/mnras/stt265](https://doi.org/10.1093/mnras/stt265)

Pop, A.-R., Hernquist, L., Nagai, D., et al. 2022, *arXiv e-prints*, arXiv:2205.11528, doi: [10.48550/arXiv.2205.11528](https://doi.org/10.48550/arXiv.2205.11528)

Rasia, E., Borgani, S., Murante, G., et al. 2015, *ApJL*, 813, L17, doi: [10.1088/2041-8205/813/1/L17](https://doi.org/10.1088/2041-8205/813/1/L17)

Rasia, E., Tripodi, R., Borgani, S., et al. 2025, *A&A*, 702, A182, doi: [10.1051/0004-6361/202554283](https://doi.org/10.1051/0004-6361/202554283)

Read, A. M., Rosen, S. R., Saxton, R. D., & Ramirez, J. 2011, *A&A*, 534, A34, doi: [10.1051/0004-6361/201117525](https://doi.org/10.1051/0004-6361/201117525)

Ruppin, F., McDonald, M., Bleem, L. E., et al. 2021, *ApJ*, 918, 43, doi: [10.3847/1538-4357/ac0bba](https://doi.org/10.3847/1538-4357/ac0bba)

Ruppin, F., McDonald, M., Hlavacek-Larrondo, J., et al. 2023, *ApJ*, 948, 49, doi: [10.3847/1538-4357/acc38d](https://doi.org/10.3847/1538-4357/acc38d)

Sabol, E. J., & Snowden, S. L. 2019, *sxrbg: ROSAT X-Ray Background Tool*, *Astrophysics Source Code Library*, record ascl:1904.001

Santos, J. S., Tozzi, P., Rosati, P., Nonino, M., & Giovannini, G. 2012, *A&A*, 539, A105, doi: [10.1051/0004-6361/201118162](https://doi.org/10.1051/0004-6361/201118162)

SAS development team. 2014, SAS: Science Analysis System for XMM-Newton observatory, *Astrophysics Source Code Library*, record ascl:1404.004

Schlafly, E. F., & Finkbeiner, D. P. 2011, *ApJ*, 737, 103, doi: [10.1088/0004-637X/737/2/103](https://doi.org/10.1088/0004-637X/737/2/103)

Schmidt, R. W., Allen, S. W., & Fabian, A. C. 2004, *MNRAS*, 352, 1413, doi: [10.1111/j.1365-2966.2004.08032.x](https://doi.org/10.1111/j.1365-2966.2004.08032.x)

Siemiginowska, A., Burke, D. J., Aldcroft, T. L., et al. 2010, *ApJ*, 722, 102, doi: [10.1088/0004-637X/722/1/102](https://doi.org/10.1088/0004-637X/722/1/102)

Singh, P., Saro, A., Costanzi, M., & Dolag, K. 2020, MNRAS, 494, 3728, doi: [10.1093/mnras/staa1004](https://doi.org/10.1093/mnras/staa1004)

Smith, R. K., Brickhouse, N. S., Liedahl, D. A., & Raymond, J. C. 2001, ApJL, 556, L91, doi: [10.1086/322992](https://doi.org/10.1086/322992)

Smith, R. K., Foster, A. R., & Brickhouse, N. S. 2012, Astronomische Nachrichten, 333, 301, doi: [10.1002/asna.201211673](https://doi.org/10.1002/asna.201211673)

Smith, R. K., Foster, A. R., Edgar, R. J., & Brickhouse, N. S. 2014, ApJ, 787, 77, doi: [10.1088/0004-637X/787/1/77](https://doi.org/10.1088/0004-637X/787/1/77)

Snowden, S. L., Freyberg, M. J., Plucinsky, P. P., et al. 1995, ApJ, 454, 643, doi: [10.1086/176517](https://doi.org/10.1086/176517)

Snowden, S. L., Egger, R., Freyberg, M. J., et al. 1997, ApJ, 485, 125, doi: [10.1086/304399](https://doi.org/10.1086/304399)

Somboonpanyakul, T., McDonald, M., Noble, A., et al. 2022, AJ, 163, 146, doi: [10.3847/1538-3881/ac5030](https://doi.org/10.3847/1538-3881/ac5030)

Stueber, H. R., Mantz, A. B., Allen, S. W., et al. 2026, arXiv e-prints, arXiv:2601.14425, doi: [10.48550/arXiv.2601.14425](https://doi.org/10.48550/arXiv.2601.14425)

Sunyaev, R. A., & Zeldovich, Y. B. 1972, Comments on Astrophysics and Space Physics, 4, 173

Suzuki, H., Plucinsky, P. P., Gaetz, T. J., & Bamba, A. 2021, A&A, 655, A116, doi: [10.1051/0004-6361/202141458](https://doi.org/10.1051/0004-6361/202141458)

Urban, O., Werner, N., Simionescu, A., Allen, S. W., & Böhringer, H. 2011, MNRAS, 414, 2101, doi: [10.1111/j.1365-2966.2011.18526.x](https://doi.org/10.1111/j.1365-2966.2011.18526.x)

Voit, G. M. 2005, Reviews of Modern Physics, 77, 207, doi: [10.1103/RevModPhys.77.207](https://doi.org/10.1103/RevModPhys.77.207)

Voit, G. M., Cavagnolo, K. W., Donahue, M., et al. 2008, ApJL, 681, L5, doi: [10.1086/590344](https://doi.org/10.1086/590344)

Walker, S., Simionescu, A., Nagai, D., et al. 2019, SSRv, 215, 7, doi: [10.1007/s11214-018-0572-8](https://doi.org/10.1007/s11214-018-0572-8)

Wan, J. T., Mantz, A. B., Sayers, J., et al. 2021, MNRAS, 504, 1062, doi: [10.1093/mnras/stab948](https://doi.org/10.1093/mnras/stab948)

White, D. A., Jones, C., & Forman, W. 1997, MNRAS, 292, 419

Wise, M. W., Davis, J. E., Huenemoerder, D. P., Houck, J. C., & Dewey, D. 2013, MARX: Model of AXAF Response to X-rays, Astrophysics Source Code Library, record ascl:1302.001

Yang, H.-Y. K., & Reynolds, C. S. 2016, ApJ, 829, 90, doi: [10.3847/0004-637X/829/2/90](https://doi.org/10.3847/0004-637X/829/2/90)

Zhuravleva, I., Churazov, E., Schekochihin, A. A., et al. 2014, Nature, 515, 85, doi: [10.1038/nature13830](https://doi.org/10.1038/nature13830)